A Test Problem for Flow Codes

Henry von Wahl, Friedrich-Schiller-Universität Jena
L. Ridgway Scott, University of Chicago

April 29, 2024

Abstract

We propose a test problem for Navier–Stokes solvers based on the flow around a cylinder. We choose a range of Reynolds numbers for which the flow is time-dependent but can be characterized as essentially two-dimensional. The test problem requires accurate resolution of chaotic dynamics over a long time interval. It also requires the use of a relatively large computational domain, part of which is curved, and it requires evaluation of derivatives of the solution and pressure on the curved boundary. We review the performance of different finite element methods for the proposed range of Reynolds numbers. These tests indicate that some of the most established methods do not capture the correct behavior.

We present a classic fluids problem, flow around a cylinder, as a challenge for numerical schemes. As reviewed in [35], there is ample experimental data with which to compare simulations. To make the challenge more tractable, we focus on 2D simulations and lower Reynolds numbers. We list some references where the computations are at variance with existing information.

Flow around a cylinder is not only a fundamental problem in fluid dynamics but also a practical problem of interest in energy generation. So-called bladeless turbines [3, 9, 11] have been proposed as a viable energy generation method. The design of such systems requires accurate simulations of the flow around cylinders.

We review some published examples where erroneous results were obtained. We also show that some commonly used techniques fail to give acceptable results at Reynolds numbers of interest. As computational simulation has emerged as a new form of experimentation in physics, it is essential to have some benchmarks that give guidance, which we use here. For many flow problems, there is no dispute regarding the Navier–Stokes equations as a suitable model, as we do here. However, this requires reliable methods to decide fundamental physics questions, such as whether the resulting flow is chaotic at a given Reynolds number.

Flow around a cylinder has been proposed as a test problem before [30, 18]. What is different here is that we focus on a range of Reynolds numbers for which the flow appears to be chaotic [35]. Thus, different metrics must be used to compare different numerical methods. Moreover, the time interval for the simulation is quite long, so this simulation evaluates the ability of different discretizations with regard to accumulation of numerical error and challenges the implementations with regard to efficiency.

We focus on simple metrics so that different methods can be compared easily. The lift and drag on a cylinder are two scalar quantities computed by many methods and measured in many experiments. Another metric is the Strouhal number or period of the time-dependent flow. In [35], a simple approach was used to estimate the periodicity of chaotic flow. We present a slightly improved method compared to [35] for evaluating the Strouhal period that provides an indication
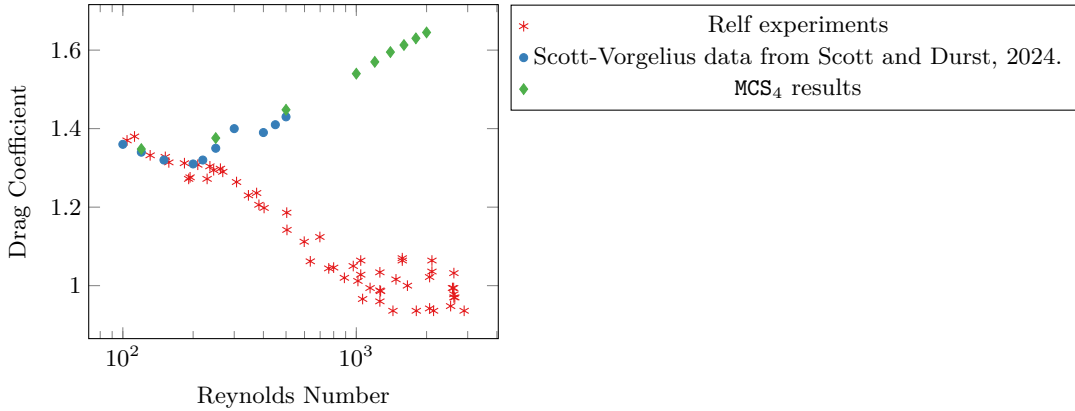
Figure 1: Relfdata compared to the data computed in [35] computed with the SV-CNAB scheme and the new data presented here.

of the transition to chaos. Additional metrics, such as the Lyapunov exponent and the fractal dimension of the attractor, provide a finer level of detail regarding the flow dynamics [35].

When the Reynolds number is more than 10^4, the flow becomes three-dimensional [17]. Thus, we restrict ourselves to Reynolds numbers in the range $[10^2, 10^4]$ for simplicity. Three-dimensional effects of a different kind are seen [38] at lower Reynolds numbers due to the finite length of cylinders used in experiments. However, these are potentially like so-called blocking effects in two-dimensional flow [29], which become less significant at higher Reynolds numbers.

In this work, We consider several methods that are well-studied and have a solid theoretical base. We compare their performance to a fifth method used in [35], and we find that the simulations in [35] were under-resolved for higher Reynolds numbers. Our main conclusion is that high-order methods are necessary to obtain reliable results at higher Reynolds numbers. Surprisingly, the commonly used, lowest-order Taylor–Hood method is not accurate enough to be used in such settings. It appears that methods that result in exactly divergence-free velocity solutions have a significant advantage at higher Reynolds numbers, even though the one we investigate is non-conforming.

One of the main conclusions from [35] was that the simulation drag values differ substantially from experiments, as shown in Figure 1. We confirm this conclusion here, suggesting that cylinder vibration likely plays a significant role in practice [39].

1 Setting the problem and model equations

Suppose that $(\mathbf{u}, p)$ is a solution of the time-dependent Navier–Stokes equations in a domain $\Omega \subset \mathbb{R}^d$ containing an obstacle with boundary $\Gamma \subset \partial\Omega$. This fulfills the equations

$$\partial_t \mathbf{u} - \nu \Delta \mathbf{u} + \mathbf{u} \cdot \nabla \mathbf{u} + \nabla p = \mathbf{0} \text{ in } \Omega,$$
$$\nabla \cdot \mathbf{u} = 0 \text{ in } \Omega, \tag{1}$$

with the kinematic viscosity ν, and together with boundary conditions

$$\mathbf{u} = \mathbf{g} \text{ on } \partial\Omega \backslash \Gamma, \quad \mathbf{u} = \mathbf{0} \text{ on } \Gamma. \tag{2}$$

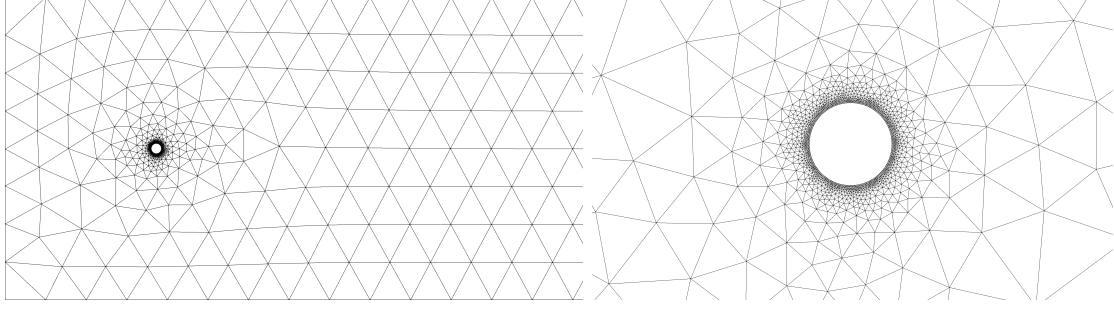For the well-posedness of these equations, see [12].

2

Figure 2: Left: Left section of mesh for the `TH` and `MCS` methods with $h = 8$. Right: Zoom in to the cylinder of the same mesh.

1.1 Problem Set-up

For our simulations, we consider the domain

$$\Omega = \left\{ (x, y) : -30 < x < 300, |y| < 30, \quad x^2 + y^2 > 1 \right\}. \tag{3}$$

The boundary condition is set as $\mathbf{g} = (1, 0)^T$ and the cylinder diameter as the reference length, the Reynolds number is given by $Re = 2/\nu$. We consider the time interval $[0, 500]$.

1.2 Weak formulation of the Navier-Stokes equations

While this test problem is not limited to finite-element simulations, we expect many will be done with finite elements. To this end, we require a variational formulation of (1). The Navier-Stokes equations can be written in a weak (or variational) form as follows:

Find $\mathbf{v} \in (H_g^1(\Omega))^d$ and $p \in L_0^2(\Omega)$ such that

$$
\begin{aligned}
(\partial_t \mathbf{u}, \mathbf{w})_{L^2(\Omega)} + a(\mathbf{u}, \mathbf{w}) + b(\mathbf{w}, p) + c(\mathbf{u}, \mathbf{u}, \mathbf{w}) = 0 \quad &\forall \mathbf{w} \in (H_0^1(\Omega))^d, \\
b(\mathbf{u}, q) = 0 \quad &\forall q \in L_0^2(\Omega).
\end{aligned}
\tag{4}
$$

The space $H_g^1(\Omega)$ is the space of H^1 functions with trace g on the (outer) boundary, $H_0^1(\Omega)$ is the space of H^1 functions with trace 0 on the boundary and $L_0^2(\Omega)$ is the space of L^2 functions with mean zero. The bilinear forms $a(\cdot, \cdot)$ and $b(\cdot, \cdot)$ are defined as

$$a(\mathbf{v}, \mathbf{w}) = \int_\Omega \frac{\nu}{2} \mathcal{D}(\mathbf{v}) : \mathcal{D}(\mathbf{w}) \, d\mathbf{x}, \qquad b(\mathbf{v}, q) = -\int_\Omega q(\nabla \cdot \mathbf{v}) \, d\mathbf{x},$$

respectively, where $\mathcal{D}(\mathbf{v}) = \nabla \mathbf{v} + \nabla \mathbf{v}^t$ and the colon (:) indicates the Frobenious inner-product of matrices. The convective (nonlinear) term takes various forms. By default, we take it to be

$$c(\mathbf{u}, \mathbf{v}, \mathbf{w}) = c_{conv}(\mathbf{u}, \mathbf{v}, \mathbf{w}) = \int_\Omega (\mathbf{u} \cdot \nabla \mathbf{v}) \cdot \mathbf{w} \, d\mathbf{x}.$$

For divergence-free functions, the various forms of the convective term are equivalent. Hence, we may take the above so-called convective form of the trilinear form for exactly divergence-free methods. However, for non-divergence-free methods, other forms are beneficial, see below.

1.3 Drag and lift evaluation

The flow of fluid around an obstacle generates a force called drag, which is a fundamental concept in fluid dynamics [22]. It plays a critical role in determining the behavior of objects in flight and has been studied since the time of d'Alembert [13]. Drag is composed of two components: pressure drag β_p and viscous drag β_v, which can be calculated by evaluating the following functions using $\mathbf{v} = (1, 0)$:

$$\beta_v(\mathbf{v}) = \oint_\Gamma \left((\nu \mathcal{D}(\mathbf{u})) \mathbf{v} \right) \cdot \mathbf{n} \, \mathrm{d}s, \qquad \beta_p(\mathbf{v}) = \oint_\Gamma -p \mathbf{v} \cdot \mathbf{n} \, \mathrm{d}s. \tag{5}$$

The full drag β is defined by $\beta = \beta_v + \beta_p$. Similarly, lift is computed using $\mathbf{v} = (0, 1)$.

1.3.1 Alternate drag evaluation

Another way [18] to evaluate β is to test the weak formulation of (1) (see (4) below) with a non-conforming test function. This results in the functional

$$\omega(\mathbf{v}) = \int_\Omega \partial_t \mathbf{u} \, \mathbf{v} \, \mathrm{d}\mathbf{x} + \int_\Omega \frac{\nu}{2} \mathcal{D}(\mathbf{u}) : \mathcal{D}(\mathbf{v}) + (\mathbf{u} \cdot \nabla \mathbf{u}) \cdot \mathbf{v} - p \nabla \cdot \mathbf{v} \, \mathrm{d}\mathbf{x}, \tag{6}$$

Then $\omega(\mathbf{v}) = \beta(\mathbf{v})$ for all $\mathbf{v} \in H^1(\Omega)^d$ [18, 14]. This form is potentially more accurate, but it requires an accurate approximation of the time derivative $\partial_t \mathbf{u}$.

This approach may be traced back to [2]. It is also known, that for the case of strongly imposed Dirichlet boundary conditions, this approach of testing the residual with a non-conforming test-function doubles the rate of convergence for the drag and lift, see, for example [4] for the proof in the steady case.

Having two ways to compute drag and lift provides a valuable internal check of the accuracy of the simulation.

2 Challenge computation

The data in Figure 1 suggests a significant disagreement between computation and experiment. This could be for a variety of reasons. The most obvious is some flaw in the computational scheme. Thus, we propose this problem as a computational challenge to see what other methods predict.

Another reason for the disagreement could be that the model is wrong. Experimentalists have raised the issue that the cylinders used could vibrate. In particular, the Relf data is based on flows past thin wires, used in musical instruments for their vibrational qualities. Thus, one response to the challenge is to allow the cylinder to vibrate back and forth in response to the oscillating lift and drag. The question would be to evaluate how oscillations of the cylinder change parameters describing the flow, such as drag, lift, and Strouhal number, representing the frequency of the generated vortices. One study with forced vibrations [25, Figure 6.9, page 179] suggests that the change could be substantial.

3 Discretization methods

The simulations in this paper are done using finite element methods. We, therefore, begin py presenting some details of the finite element approach.

To discretize the weak formulation (4) with finite element methods, we take a mesh of the domain Ω with characteristic length h, denoted as $\mathcal{T}_h$. Finite element spaces then look to discretize (4) by approximating the spaces $H^1(\Omega)$ and $L^2(\Omega)$ with spaces of piecewise polynomials on each element of the mesh, with varying degree of discontinuity of these polynomials over element edges.

We utilize two well-established simulation methods for which extensive numerical analysis is available, establishing not only convergence but also detailed simulation properties.

3.1   H(div) conforming finite element discretization

We consider an $H(\text{div})$-conforming finite element method based on [16, 15]. This discretization is based on mass-conserving mixed formulation with symmetric stresses, also known as the MCS formulation. This approach discretizes the velocity in $H(\text{div})$ using Brezzi–Douglas–Marini (BDM) elements [34]. That is, the normal component of the velocity is continuous across element boundaries, while the tangential component is discontinuous. The pressure is discretized using discontinuous elements. This method is exactly mass conserving and pressure-robust. From a numerical point of view, pressure-robust methods have several advantages. First, the velocity remains unchanged by irrotational changes in any external forcing term, a property that most methods do not preserve on the discrete level [23]. More importantly, pressure-robust methods have the property that the velocity error is independent of the pressure error [20]. This contrasts classical Galerkin discretizations of the (Navier)-Stokes equations, where the velocity error depends on $\frac{1}{\nu}$ times the pressure error. From a physical point of view, exactly divergence-free methods have the advantage that, in addition to mass, kinetic energy, linear momentum, and angular momentum are conserved on the discrete level [6, 33].

Furthermore, this method is based on a formulation where an additional variable $\sigma = \nu \nabla \mathbf{u}$ which is discretised in the function space $H(\text{curl div})$. Thus the energy form is modified to

$$a'(\sigma, \tau) = \frac{1}{\nu} \int_\Omega \sigma : \tau \, d\mathbf{x},$$

and a new form is defined:

$$b'(\tau, \mathbf{u}) = \sum_{T \in \mathcal{T}_h} \int_T \nabla \cdot (\tau) \cdot \mathbf{u} \, d\mathbf{x} + \sum_{e \in \mathcal{T}_h} \int_e [\tau_{nn}] \mathbf{u} \cdot \mathbf{n} \, ds,$$

where $\mathcal{T}_h$ is the triangular mesh, T denotes triangles in $\mathcal{T}_h$, and e denotes edges in $\mathcal{T}_h$. The expression $[\tau_{nn}]$ denotes the jump in the normal-normal component of the tensor τ across the edge e, and $\mathbf{n}$ is the normal to the edge. Note that the orientation of the normal is not material. Thus the formulation is

$$\begin{aligned} a'(\sigma_h, \tau_h) + b'(\tau_h, \mathbf{u}_h) &= 0 \quad \forall \tau_h \in \Sigma_h, \\ (\partial_t \mathbf{u}_h, \mathbf{v}_h)_{L^2(\Omega)} + b'(\sigma_h, \mathbf{v}_h) + c(\mathbf{u}_h, \mathbf{u}_h, \mathbf{v}_h) + b(\mathbf{v}_h, p_h) &= 0 \quad \forall \mathbf{v}_h \in V_h, \\ b(\mathbf{u}_h, q_h) &= 0 \quad \forall q_h \in Q_h. \end{aligned} \quad (7)$$

Here, Σ_h is a space of discontinuous piecewise polynomials of degree k, whose values are trace-zero tensors satisfying continuity of the 'normal-tangential component' across edges and that the normal-tangential component is a polynomial of order $k-1$ on each edge, V_h denotes the BDMk finite-element space of order k, and Q_h consists of discontinuous piecewise polynomials of degree $k-1$.

As $H(\mathrm{div})$ spaces are characterized by normal continuity across facets, boundary condition in the normal components are imposed strongly. The implementation used uses hybridisation for the tangential component of the velocity. That is, a second finite element space is used to couple the tangential component across element facets and the tangential part of the boundary condition is enforced strongly on the facet space.

For time-stepping we use a second order IMEX scheme known as SBDF2 [1]. This scheme uses the BDF2 scheme to discretise the time-derivative, the Stokes term is fully implicit, and the non-linear convective term is treated explicitly with a second order extrapolation:

$$a'(\sigma_h^n, \tau_h) + b'(\tau_h, \mathbf{u}_h^n) = 0 \quad \forall \tau_h \in \Sigma_h, \tag{8a}$$

$$\tfrac{1}{\Delta t}(\tfrac{3}{2}\mathbf{u}_h^n - 2\mathbf{u}_h^{n-1} + \tfrac{1}{2}\mathbf{u}_h^{n-2}, \mathbf{v}_h)_{L^2(\Omega)} + b'(\sigma_h^n, \mathbf{v}_h) + b(\mathbf{v}_h, p_h^n)$$
$$+ 2c(\mathbf{u}_h^{n-1}, \mathbf{u}_h^{n-1}, \mathbf{v}_h) - c(\mathbf{u}_h^{n-2}, \mathbf{u}_h^{n-2}, \mathbf{v}_h) = 0 \quad \forall \mathbf{v}_h \in V_h, \tag{8b}$$

$$b(\mathbf{u}_h^n, q_h) = 0 \quad \forall q_h \in Q_h. \tag{8c}$$

To regularize the saddle-point system and to fix the pressure constant in the case of pure Dirichlet boundary conditions, we may add a small perturbation to the lower right pressure block of the block-system resulting from (8). That is, we modify (8c) to

$$-\int_\Omega q_h(\nabla \cdot \mathbf{u}_h^n) + \epsilon \int_\Omega p_h^n q_v \, \mathrm{d}\mathbf{x} = -\int_\Omega q_h((\nabla \cdot \mathbf{u}_h^n) - \epsilon p_h^n) \, \mathrm{d}\mathbf{x} = 0, \quad \forall q_h \in Q_h, \tag{9}$$

with some $\epsilon > 0$. Since our discrete spaces V_h, Q_h satisfy the discrete de-Rahm complex [20], we have the property that $\nabla \cdot V_h = Q_h$. Consequently, we can replace q_h with $\nabla \cdot \mathbf{v}_h$ in (9). This gives us an equation for the pressure, which we may plug into the second equation in (8). This leads to the discrete system,

$$a'(\sigma_h^n, \tau_h) + b'(\tau_h, \mathbf{u}_h^n) + \tfrac{1}{\Delta t}(\tfrac{3}{2}\mathbf{u}_h^n, \mathbf{v}_h)_{L^2(\Omega)} + b'(\sigma_h^n, \mathbf{v}_h) - b(\mathbf{v}_h, \tfrac{1}{\epsilon}\nabla \cdot \mathbf{u}_h). \tag{10}$$

This is a smaller linear system to solve, and the system is no longer a saddle point problem, making it an easier system to solve numerically. We want to choose ϵ small to keep the perturbation from the divergence constraint small. However, this means that the $\frac{1}{\epsilon}$-scaled term causes the linear system (10) to be very ill-conditioned. Consequently, we need to use direct linear solvers to handle these ill-conditioned linear systems, which in turn limits us with respect to the maximal size of the system we can solve and the parallel scalability. With the small perturbation, the divergence of $\mathbf{u}_h$ is no longer exactly zero, but $\|\nabla \cdot \mathbf{u}_h^n\|_{L^2} \leq \epsilon \|p_h^n\|_{L^2}$. In the computations, we chose $\epsilon = 10^{-12}/\nu$.

We will refer to approach above as $\mathtt{MCS}_k$, where k is the order of the velocity finite element space. This approach is implemented using Netgen/NGSolve [31, 32] and based on a template available on github[1].

3.2 Taylor-Hood

To compare with more established methods, we also consider Taylor-Hood elements consisting of H^1-conforming finite elements of order $k \geq 2$ for the velocity and order $k - 1$ for the pressure.

To stabilize this scheme, we optionally add grad-div stabilisation to improve the conservation of mass[26, 7]. That is, we add the term

$$j_h(\mathbf{u}_h, \mathbf{v}_h) := \gamma_{gd} \int_\Omega \nabla \cdot \mathbf{u}_h \nabla \cdot \mathbf{v}_h \, \mathrm{d}\mathbf{x}, \tag{11}$$

---

[1] https://github.com/NGSolve/modeltemplates

to our bilinear form. In our computations, we take $\gamma_{gd} = 10^3$, and we refer to this method as $\texttt{gdTH}_k$, where k is the order of the velocity space. In case no grad-div stabilization is used, we refer to the method as $\texttt{TH}_k$. Furthermore, we note that it is known that for $\gamma_{gd} \to \infty$, the grad-div stabilized Taylor-Hood solution converges to the Scott-Vogelius solution [5, 24].

For the convective term, there are multiple choices possible, we take the divergence form [19],

$$c_{div}(\mathbf{u}, \mathbf{v}, \mathbf{w}) = c_{conv}(\mathbf{u}, \mathbf{v}, \mathbf{w}) + \frac{1}{2} \int_\Omega (\nabla \cdot \mathbf{u}) \mathbf{v} \cdot \mathbf{w} \, d\mathbf{x}, \tag{12}$$

which is equivalent to the standard convective form on the continuous level, but vanishes under less restrictive conditions for $\mathbf{v} = \mathbf{w}$ on the discrete level.

Thus the variational formulation takes the form

$$(\partial_t \mathbf{u}_h, \mathbf{w}_h)_{L^2(\Omega)} + a(\mathbf{u}_h, \mathbf{w}_h) + j_h(\mathbf{u}_h, \mathbf{w}_h) + b(\mathbf{w}_h, p_h) + c_{div}(\mathbf{u}_h, \mathbf{u}_h, \mathbf{w}_h) = 0 \quad \forall \mathbf{w}_h \in V_h,$$
$$b(\mathbf{u}_h, q_h) = 0 \quad \forall q_h \in Q_h, \tag{13}$$

where V_h is the standard Lagrange space of continuous, piecewise polynomials of degree $k \geq 2$, and Q_h is the standard Lagrange space of continuous, piecewise polynomials of degree $k - 1$.

To discretise in time-we use the fully implicit Crank-Nicolson scheme, that is

$$\frac{1}{\Delta t}(\mathbf{u}_h^n - \mathbf{u}_h^{n-1}, \mathbf{w}_h)_{L^2(\Omega)} + \frac{1}{2}\Big(a(\mathbf{u}_h^n, \mathbf{w}_h) + c_{div}(\mathbf{u}_h^n, u_h^n, \mathbf{w}_h)\Big) + j_h(\mathbf{u}_h^n, \mathbf{w}_h) + b(\mathbf{w}_h, p_h^n)$$
$$+ \frac{1}{2}\Big(a(\mathbf{u}_h^{n-1}, \mathbf{w}_h) + c_{div}(\mathbf{u}_h^{n-1}, \mathbf{u}_h^{n-1}, \mathbf{w}_h)\Big) = 0 \quad \forall \mathbf{w}_h \in V_h,$$
$$b(\mathbf{u}_h^n, q_h) = 0 \quad \forall q_h \in Q_h, \tag{14}$$

Note that we do not take into account the pressure from the previous time step, nor do we add the grad-div stabilization term from the last time step. This is because the method needs to correctly reflect that the is Langrange-multiplier to weakly enforce the divergence constraint [28, Section 4.1.4]. Similarly, the grad-div form is also there to penalize deviations from the divergence constraint.

We use a quasi-Newton method with line search to solve the nonlinear systems arising in every time step. More precisely, we only recompute the factorization of the inverse Jacobi-matrix if the residual decreases by less than a factor of 0.3. The line search consists of a check that the Newton update has decreased the residual. Otherwise, we reduce the size of the update by half recursively until the residual has decreased compared to the previous iteration. We start each quasi-Newton iteration with (u_h, p_h) from the previous time step. As the scheme is fully implicit, we can use time steps independent of the mesh size, and as the Jacobi-matrix rarely has to be refactorized, the method is essentially as efficient as IMEX schemes.

The Taylor–Hood methods are also implemented using Netgen/NGSolve. The meshes used are constructed as those for the $H(\text{div})$-conforming method in Section 3.1.

3.3 Scott–Vogelius

As a final method, we also consider the Scott–Vogeluis finite element pair. This finite element pair is very similar to the Taylor–Hood pair, using H^1-conforming finite elements for the velocity but discontinuous elements of order $k - 1$ for the pressure. Consequently, we use the same variational formulation time-stepping scheme used for the unstabilized Taylor-Hood method. For $k \geq 4$ in two dimensions, this method is inf-sup stable on meshes without nearly singular vertices [37, 36] and

for $k \geq d = 2$ on barycentric refined meshes [27, 40]. This method is also exactly divergence-free and pressure-robust.

There are different ways that the Scott–Vogelius method [34] can be implemented. In [35], the iterated penalty method was used to avoid explicit knowledge of the pressure space. However, this approach was plagued by nearly singular vertices [14] in the meshes used. Here, we utilize the Netgen mesh generator, which, for the cylinder problem, does not have any singular or nearly singular vertices. Thus, the mixed-method implementation of Scott–Vogelius can be used, and in this case, there is only one change from the (unstabilized) Taylor–Hood method, namely, the pressure elements are discontinuous instead of continuous. One drawback of this approach is the linear systems are larger, and it appears that for Reynolds number 8000 (Table 7), it is no longer possible to keep the divergence very small. Upon closer examination, it was found that the Newton step was not converging at a few time steps, and the divergence also spiked there. In general, the divergence was very small except at these few times. Furthermore, it is worth mentioning that, unlike the unstabilized Taylor-Hood method, the lack of convergence of Newton's method did not lead to a blow-up of the solution.

3.4 Meshes

We used several meshes for our experiments. For the methods described in Section 3, the meshes are unstructured simplicial meshes constructed using Netgen [31] using a bulk mesh parameter h_{max} and a local mesh size $h_{min} = h_{max}/250$ on the boundary of the cylinder. The part of the coarsest mesh ($h_{max} = 8$) around the cylinder is visualized in Figure 2.

For $h_{max} = 8, 4, 2$, the Taylor-Hood finite element space has a total of 6994, 163107, and 437439 degrees of freedom (dofs), respectively, for the saddle point system. The Scott-Vogelius saddle point systems have 87858, 205176, and 551434 dofs, respectively, due to the larger pressure space. On the same meshes, the MSC method has 95856, 224487, and 604047 dofs for the stress and velocity space in which we solve the problem. However, we emphasize that a direct comparison of dofs is not appropriate, as different types of systems must be solved for each method, and the methods have significant differences regarding their approximation power.

3.5 Computing the period

Following [35], we estimate the period of the drag-lift trajectory as follows. For selected points along the trajectory (about 100 per period), we consider points from roughly one-half period away to three-halfs away and determine the point of closest approach. We start with an estimated average period, and for each initial point we, obtain an estimated period. Histograms of such estimates are given in Figure 6. Taking the average period from this data gives an estimate of the Strouhal period that can be used to refine the process, providing a new estimated average period. To allow for estimates of the period at a finer grain than the individual time steps, we used a quadratic interpolation of estimated periods to allow for prediction of the period to second order. That is, we found the trajectory error at the optimal point and then considered the error at the time steps on either side of this. Fitting this data with a quadratic and finding the minimum of the quadratic provided an estimated period to within a fraction of Δt.
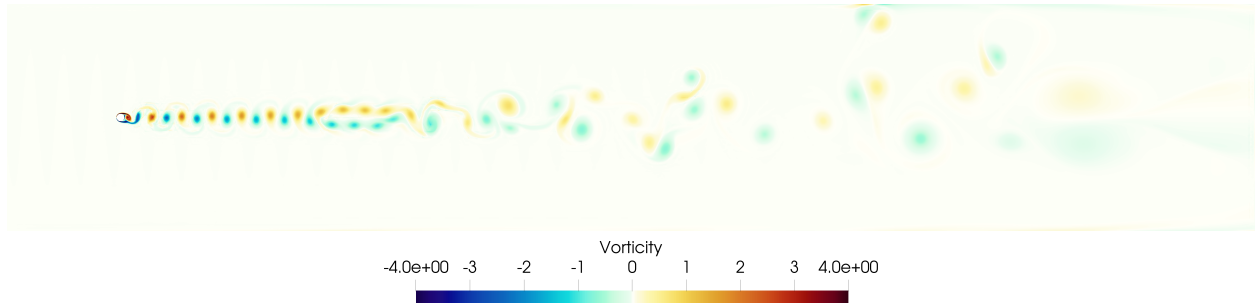
Figure 3: Vorticity of the flow with Reynolds number 500 at $t = 300$ computed using the `MCS`$_4$ method on the mesh with $h_{\max} = 2$.

4 Computational experiments

We consider Reynolds numbers between 120 and 8000. The results for Reynolds numbers 120, 250, 500, 1000, 2000, 4000, and 8000 are shown in Table 1, Table 2, Table 3, Table 4, Table 5, Table 6, and Table 7, respectively. Furthermore, results for Reynolds numbers between 1100 and 1800 are shown in Table 8. Finally, the vorticity of the resulting flow computed on the finest mesh with the MSC method is shown for Reynolds numbers 500, 1000, and 2000 in Figure 3, Figure 4, and Figure 5, respectively.

4.1 Reynolds 120–500

We began with a small Reynolds number (120) to provide a low bar for diverse methods. Nevertheless, Table 1 shows that unstabilized, low-order ($k = 2$) Taylor–Hood, which is commonly thought of as the workhorse for fluid flow, struggled to get a viable result. By contrast, all of the high-order methods agree to several digits in the prediction of the Strouhal period and drag. The stabilized Taylor–Hood for $k = 2$ is between the high-order predictions and the unstabilized $k = 2$ results. Note that at this Reynolds number, stabilization of high-order ($k = 4$) Taylor–Hood does not make a difference, except on the size of the divergence error.

Table 2 tells a similar story with Reynolds number 250. The high-order methods are in agreement and the low-order methods are substandard, in particular suggesting chaotic behavior.

For Reynolds numbers 500 and higher, we decided to drop the lowest-order Taylor–Hood simulation data. This is due to the method's poor performance at the lower Reynolds numbers. In some cases, the unstabilized did not even continue to time 500, with the Newton iteration failing and the solution blowing up. For Reynolds number 500, c.f. Table 3, even the stabilized lowest-order Taylor–Hood simulation data is not viable. For higher Reynolds numbers, we no longer report results using this method. Finally, the vorticity of the velocity solution from the MCS method on the finest mesh is shown in Figure 3. Here, we see the periodic flow in the wake of the cylinder for about 70 spatial units, after which the flow transitions away into more chaotic behavior. However, since our mesh is very coarse in this part of the domain, compared to the resolution around the cylinder, we do not claim that this is the fully resolved behavior so far downstream in the channel.

4.2 Reynolds 1000 and higher

For Reynolds numbers 1000 and higher, only three methods remain viable: the pressure-robust MSC and Scott–Vogelius methods, and the grad-div stabilized high-order Taylor–Hood method.

Method	$h_{\max}$ / $h_{\min}$	Δt	t_{start}	t_{end}	Drag	Period	$\|\nabla \cdot \mathbf{u}_h\|_{\ell^\infty(L^2(\Omega))}$
MCS$_4$	8 / 0.032	0.005	280	480	1.3486	11.339 ± 0.00073	NA
MCS$_4$	4 / 0.016	0.0025	280	480	1.3485	11.337 ± 0.00085	NA
MCS$_4$	2 / 0.008	0.00125	280	480	1.3482	11.337 ± 0.00098	NA
SV$_4$	8 / 0.032	0.01	280	480	1.3542	11.303 ± 0.00354	2.83×10^{-7}
gdTH$_4$	8 / 0.032	0.01	280	480	1.3541	11.304 ± 0.00350	3.44×10^{-3}
gdTH$_4$	4 / 0.016	0.01	280	480	1.3492	11.339 ± 0.00005	1.52×10^{-3}
gdTH$_4$	2 / 0.008	0.01	280	480	1.3476	11.338 ± 0.00010	5.72×10^{-4}
gdTH$_2$	8 / 0.032	0.01	280	480	1.4633	11.139 ± 0.28907	1.35×10^{-2}
gdTH$_2$	4 / 0.016	0.01	280	480	1.3222	11.814 ± 0.05813	1.10×10^{-2}
TH$_4$	8 / 0.032	0.01	280	480	1.3443	11.379 ± 0.00049	3.74×10^{0}
TH$_4$	4 / 0.016	0.01	280	480	1.3492	11.339 ± 0.00005	2.57×10^{0}
TH$_2$	8 / 0.032	0.01	280	380	1.1136	9.518 ± 3.01488	8.61×10^{1}
TH$_2$	4 / 0.016	0.01	280	480	1.0662	7.898 ± 2.89044	5.42×10^{0}
TH$_2$	2 / 0.008	0.01	280	480	1.2397	9.368 ± 2.66038	2.35×10^{0}

Table 1: Reynolds number 120. The consensus values for the average drag is 1.348 and for the Strouhal period is 11.34.

Method	$h_{\max}$ / $h_{\min}$	Δt	t_{start}	t_{end}	Drag	Period	$\|\nabla \cdot \mathbf{u}_h\|_{\ell^\infty(L^2(\Omega))}$
MCS$_4$	8 / 0.032	0.005	280	480	1.3750	9.681 ± 0.00011	NA
MCS$_4$	4 / 0.016	0.0025	280	480	1.3769	9.673 ± 0.00013	NA
MCS$_4$	2 / 0.008	0.00125	280	480	1.3760	9.680 ± 0.00023	NA
gdTH$_4$	8 / 0.032	0.01	280	480	1.3867	9.658 ± 0.01316	5.77×10^{-3}
gdTH$_4$	4 / 0.016	0.01	280	480	1.3749	9.679 ± 0.00007	3.84×10^{-3}
gdTH$_4$	2 / 0.008	0.01	280	480	1.3765	9.684 ± 0.00009	1.21×10^{-3}
gdTH$_2$	8 / 0.032	0.01	280	480	1.3531	9.460 ± 1.79078	1.67×10^{-2}
gdTH$_2$	4 / 0.016	0.01	280	480	1.3529	9.732 ± 0.35677	1.47×10^{-2}
TH$_2$	2 / 0.008	0.01	280	480	1.0144	9.488 ± 2.64040	1.22×10^{2}

Table 2: Reynolds number 250. The consensus values for the average drag is 1.376 and for the Strouhal period is 9.680.

Method	$h_{\max}$ / $h_{\min}$	Δt	t_{start}	t_{end}	Drag	Period	$\|\nabla \cdot \mathbf{u}_h\|_{\ell^\infty(L^2(\Omega))}$
MCS$_4$	8 / 0.032	0.002	280	480	1.4464	8.836 ± 0.00004	NA
MCS$_4$	4 / 0.016	0.001	280	480	1.4499	8.811 ± 0.00006	NA
MCS$_4$	2 / 0.008	0.0005	280	480	1.4477	8.822 ± 0.00016	NA
gdTH$_4$	8 / 0.032	0.01	280	450	1.4537	8.823 ± 0.43717	7.82×10^{-3}
gdTH$_4$	4 / 0.016	0.01	280	480	1.4488	8.877 ± 0.00796	4.77×10^{-3}
gdTH$_4$	2 / 0.008	0.01	280	480	1.4483	8.811 ± 0.00007	2.85×10^{-3}
gdTH$_2$	8 / 0.032	0.01	280	480	1.3838	8.966 ± 1.90009	2.09×10^{-2}
gdTH$_2$	4 / 0.016	0.01	280	480	1.3753	8.716 ± 1.20772	1.82×10^{-2}

Table 3: Reynolds number 500. The consensus values for the average drag is 1.448 and for the Strouhal period is 8.82.

The results are presented in Table 4 for Reynolds number 1000. Additionally, the vorticity of the MSC method on the finest mesh at time $t = 300$ is shown in Figure 4.

At Reynolds number 1000, the drag-lift dynamics are very close to periodic but have a very small standard deviation in the computed period. In particular, we see in Figure 4 that the solution remains periodic for about 40 units downstream of the cylinder before the solution transitions into chaos. However, we again cannot claim high accuracy of the solution in this part of the domain, compared to close to the cylinder. Furthermore, the $\mathtt{gdTH}_4$ and $\mathtt{SV}_4$ drag-lift dynamics are only periodic on the finest mesh considered. Nevertheless, the Scott–Vogelius method on the second mesh presents a significantly smaller standard deviation of the Strouhal period compared to the solution of the stabilized Taylor–Hood method. Overall, it is harder to get a close agreement for the average drag and even harder for the Strouhal period at this and higher Reynolds numbers.

In Table 5, we see for Reynolds number 2000 that the drag-lift dynamics is no longer periodic, as also observed in [8]. Similar to [8, Fig. 7], we observe an oscillation of the wake of the flow behind the cylinder in Figure 5.

As the drag-lift dynamics is no longer periodic at Reynolds number 2000, we computed the flow for a sequence of Reynolds number values between 1000 and 2000 to see how the chaos emerges, as shown in Table 8. We obtain a plausibly periodic solution at Reynolds number 1125, but with an ever-increasing standard deviation of the Strouhal period as the Reynolds number increases, even on the finest meshes.

For Reynolds numbers 4000 and higher, we no longer attempt to provide consensus values for the Strouhal period or drag; see Table 6 and Table 7. Furthermore, Figure 6 illustrates how the spread in the computed Strouhal period increases with increasing Reynolds number.

4.2.1 Better to be div-zero than conforming?

As far as we are aware, there are no direct comparisons between conforming and non-conforming pressure-robust methods, so our results give some data on this issue. A direct comparison between fully discontinuous Galerkin and a $H(\mathrm{div})$-conforming method was performed in [10]. Our results indicate that the $H(\mathrm{div})$-conforming MCS method is slightly better than stabilized Taylor–Hood in many cases. This suggests that there is an advantage to being exactly divergence-zero, with little penalty due to the nonconformity of the velocity. This may be because the MCS method, like Scott–Vogelius, is pressure robust, i.e., the velocity error is independent of the pressure error. On the other hand, for Reynolds number 4000 (Table 6), we see that the MCS predictions have a significant variation with regard to mesh variation. The Scott–Vogelius predictions tend to be smaller than Taylor–Hood. For Reynolds number 8000 (Table 7), we see that the MCS prediction for the average drag coefficient differs significantly from the Scott–Vogelius and Taylor–Hood predictions. However, as noted above, the Newton iteration failed to converge in a few time steps in the Scott–Vogelius computation, although it did converge in the stabilized Taylor–Hood simulation.

5 Other methods

We survey briefly other methods that have been used for simulating flow around a cylinder.

Method	$h_{\max}$ / $h_{\min}$	Δt	t_{start}	t_{end}	Drag	Period	$\|\nabla \cdot \mathbf{u}_h\|_{\ell^\infty(L^2(\Omega))}$
MCS$_4$	8 / 0.032	0.001	280	480	1.5420	8.351 ± 0.00005	NA
MCS$_4$	4 / 0.016	0.0005	280	480	1.5504	8.322 ± 0.00036	NA
MCS$_4$	4 / 0.016	0.00025	280	480	1.5384	8.361 ± 0.00318	NA
gdTH$_4$	8 / 0.032	0.01	280	480	1.5343	8.481 ± 1.30527	1.07×10^{-2}
gdTH$_4$	4 / 0.016	0.01	280	480	1.5162	8.297 ± 0.42448	6.79×10^{-3}
gdTH$_4$	4 / 0.016	0.005	280	480	1.5163	8.302 ± 0.41216	6.78×10^{-3}
gdTH$_4$	2 / 0.008	0.01	280	480	1.5444	8.365 ± 0.00169	5.13×10^{-3}
SV$_4$	8 / 0.032	0.01	280	480	1.5400	8.550 ± 1.31361	9.78×10^{-6}
SV$_4$	4 / 0.016	0.01	280	480	1.5168	8.278 ± 0.24277	4.40×10^{-7}
SV$_4$	2 / 0.008	0.01	280	480	1.5444	8.365 ± 0.00157	1.18×10^{-7}

Table 4: Reynolds number 1000. The consensus values for the average drag is 1.54 and for the Strouhal period is 8.36.
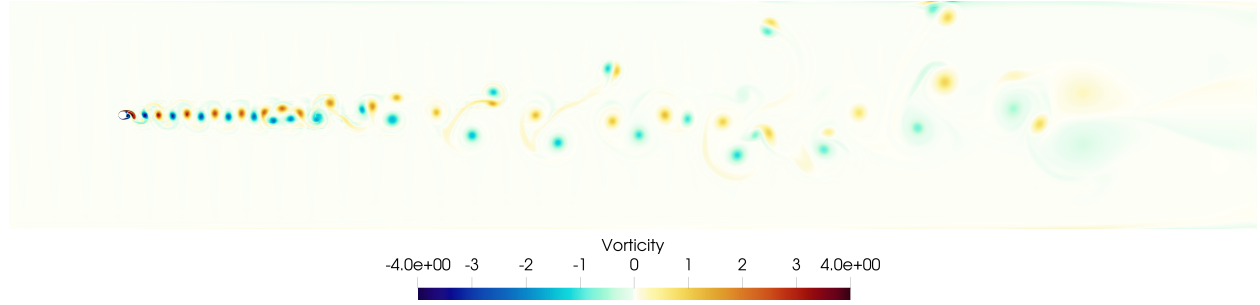
Figure 4: Vorticity of the flow with Reynolds number 1000 at $t = 300$ computed using the MCS$_4$ method on the mesh with $h_{\max} = 2$.

Method	$h_{\max}$ / $h_{\min}$	Δt	t_{start}	t_{end}	Drag	Period	$\|\nabla \cdot \mathbf{u}_h\|_{\ell^\infty(L^2(\Omega))}$
MCS$_4$	8 / 0.032	0.001	280	480	1.6447	8.441 ± 0.99875	NA
MCS$_4$	4 / 0.016	0.0005	280	480	1.6470	8.417 ± 0.95675	NA
MCS$_4$	2 / 0.008	0.00025	280	480	1.6411	8.407 ± 0.94202	NA
SV$_4$	2 / 0.008	0.01	280	480	1.6603	8.066 ± 0.68569	1.75×10^{-7}
gdTH$_4$	4 / 0.016	0.01	280	480	1.5798	8.902 ± 1.27449	9.55×10^{-3}
gdTH$_4$	2 / 0.008	0.01	280	480	1.6524	8.365 ± 0.96296	5.61×10^{-3}

Table 5: Reynolds number 2000. The consensus values for the average drag is 1.65 and for the Strouhal period is 8.4.

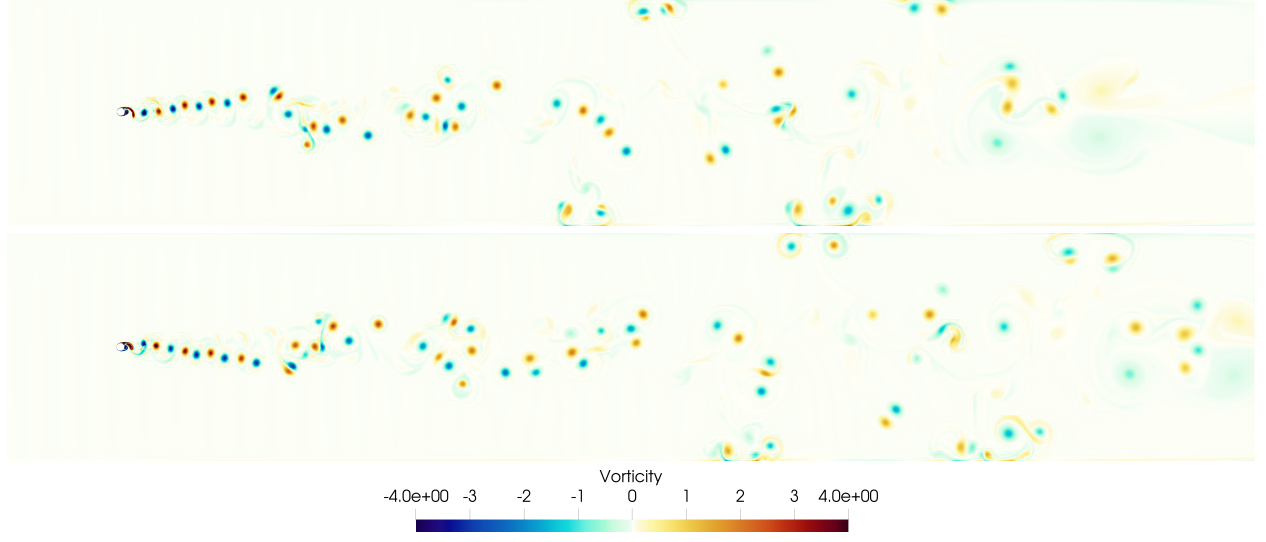| Method	$h_{\max}$ / $h_{\min}$	Δt	t_{start}	t_{end}	Drag	Period	$\|\nabla \cdot \mathbf{u}_h\|_{\ell^\infty(L^2(\Omega))}$
MCS$_4$	8 / 0.032	0.001	280	480	1.7778	7.867 ± 1.32713	NA
MCS$_4$	4 / 0.016	0.0005	280	480	1.5922	9.030 ± 2.33259	NA
MCS$_4$	2 / 0.008	0.00025	280	480	1.7717	7.792 ± 1.32658	NA
SV$_4$	2 / 0.008	0.01	280	480	1.4719	8.904 ± 2.68945	1.28×10^{-6}
gdTH$_4$	4 / 0.016	0.01	280	480	1.6283	8.941 ± 2.01980	1.25×10^{-2}
gdTH$_4$	2 / 0.008	0.01	280	480	1.5620	8.997 ± 2.61238	9.48×10^{-3}

Table 6: Reynolds number 4000.

Figure 5: Vorticity of the flow with Reynolds number 2000 computed using the `MCS4` method on the mesh with $h_{\max} = 2$. Top: $t = 310$, Bottom: $t = 350.4$.

Method	$h_{\max}\,/\,h_{\min}$	Δt	t_{start}	t_{end}	Drag	Period	$\lVert \nabla \cdot \mathbf{u}_h \rVert_{\ell^\infty(L^2(\Omega))}$
MCS$_4$	4 / 0.016	0.0004	280	480	1.6900	8.924 ± 2.46617	NA
MCS$_4$	2 / 0.008	0.0002	280	480	1.7262	9.252 ± 2.32805	NA
SV$_4$	2 / 0.008	0.01	280	480	1.6481	9.353 ± 2.23443	3.52×10^{-3}
gdTH$_4$	4 / 0.016	0.01	280	480	1.5174	8.883 ± 2.27784	1.29×10^{-2}
gdTH$_4$	2 / 0.008	0.01	280	480	1.6522	9.135 ± 2.38565	1.17×10^{-2}

Table 7: Reynolds number 8000

Reynolds number	Method	$h_{\max}\,/\,h_{\min}$	Δt	t_{start}	t_{end}	Drag	Period
1100	MCS$_4$	8 / 0.032	0.001	280	480	1.5581	8.279 ± 0.00258
1125	MCS$_4$	8 / 0.032	0.001	280	480	1.5628	8.262 ± 0.00822
1150	MCS$_4$	8 / 0.032	0.001	280	480	1.5660	8.245 ± 0.02200
1175	MCS$_4$	8 / 0.032	0.001	280	480	1.5718	8.230 ± 0.07870
1200	MCS$_4$	8 / 0.032	0.001	280	480	1.5743	8.206 ± 0.33194
1200	MCS$_4$	4 / 0.016	0.0005	280	480	1.5811	8.245 ± 0.91742
1200	MCS$_4$	2 / 0.008	0.00025	280	480	1.5728	8.227 ± 0.48112
1400	MCS$_4$	8 / 0.032	0.001	280	480	1.5961	8.534 ± 1.07792
1400	MCS$_4$	4 / 0.016	0.0005	280	480	1.5947	8.576 ± 1.17649
1400	MCS$_4$	2 / 0.008	0.00025	280	480	1.5959	8.536 ± 1.11533
1600	MCS$_4$	8 / 0.032	0.001	280	480	1.6103	8.520 ± 1.15913
1600	MCS$_4$	4 / 0.016	0.005	280	480	1.6137	8.504 ± 1.16444
1600	MCS$_4$	2 / 0.008	0.0025	280	480	1.6136	8.507 ± 1.05176
1800	MCS$_4$	8 / 0.032	0.001	280	480	1.6312	8.462 ± 1.00298
1800	MCS$_4$	4 / 0.016	0.005	280	480	1.6305	8.475 ± 1.06059
1800	MCS$_4$	2 / 0.008	0.0025	280	480	1.6327	8.481 ± 0.98248

Table 8: Investigating at what Reynolds number the flow becomes chaotic.

13

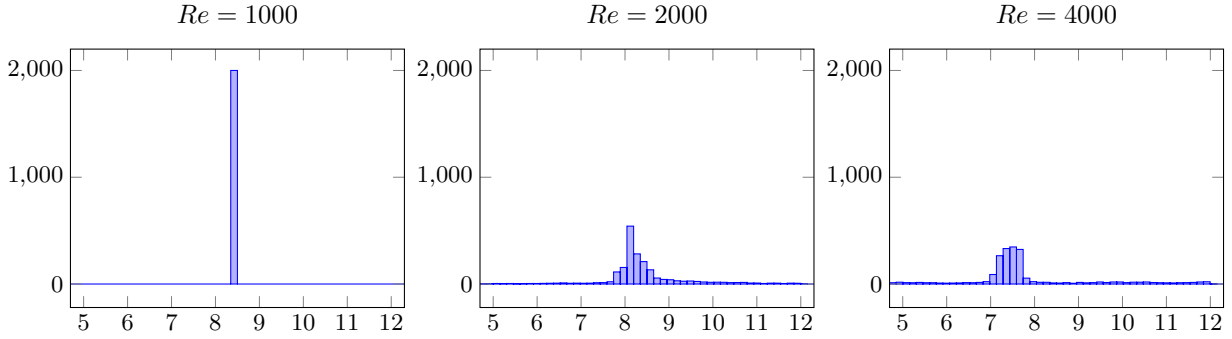Figure 6: Histogram of the computed periods of the flow at Reynolds numbers 1000, 2000, 4000 using the `MCS`$_4$ method with $h_{\max} = 2$.

5.1 Vortex blob

The publication [8, Figure 5] suggests that drag and lift for flow around a cylinder is nearly periodic at $R = 1000$, in agreement with our findings, with chaotic flow for $R \geq 2000$.

5.2 OpenFoam

OpenFoam may not be the ideal discretization approach for low Reynolds numbers. In [21], Strouhal numbers and frequencies computed with OpenFoam were found to be in error by greater than a factor of two for $R \in [55, 161]$.

6 Conclusions

We considered several finite element methods for solving flow past a cylinder. All of these methods are well studied both computationally and theoretically. We found that high-order and pressure-robust methods are necessary to obtain reliable results at higher Reynolds numbers. The widely-used, lowest-order Taylor–Hood method was not accurate enough to give appropriate results. We were able to confirm some earlier results by other researchers. Exact incompressibility appears to be important at higher Reynolds numbers, even though the one such method that we investigated is non-conforming. We studied in detail how chaos appears to emerge for Reynolds numbers just above 1000.

Data Availability Statement

The code used to realize the presented results, the raw data generated by this code and videos of key simulations are available on zenodo at https://doi.org/10.5281/zenodo.11068455.

Acknowledgments

References

[1] U. M. Ascher, S. J. Ruuth, and B. T. R. Wetton. Implicit-explicit methods for time-dependent partial differential equations. *SIAM J. Numer. Anal.*, 32(3):797–823, 1995. doi:10.1137/0732037.

[2] I. Babuška and A. Miller. The post-processing approach in the finite element method—part 1: calculation of displacements, stresses and other higher derivatives of the displacements. *Internat. J. Numer. Methods Engrg.*, 20(6):1085–1109, 1984. doi:10.1002/nme.1620200610.

[3] I. Bahadur. Dynamic modeling and investigation of a tunable vortex bladeless wind turbine. *Energies*, 15(18): 6773, 2022. doi:10.3390/en15186773.

[4] M. Braack and T. Richter. Solutions of 3D Navier–Stokes benchmark problems with adaptive finite elements. *Comput. Fluids*, 35(4):372–392, 2006. doi:10.1016/j.compfluid.2005.02.001.

[5] M. A. Case, V. J. Ervin, A. Linke, and L. G. Rebholz. A connection between Scott–Vogelius and grad-div stabilized Taylor–Hood FE approximations of the Navier–Stokes equations. *SIAM J. Numer. Anal.*, 49(4): 1461–1481, 2011.

[6] S. Charnyi, T. Heister, M. A. Olshanskii, and L. G. Rebholz. On conservation laws of Navier-Stokes Galerkin discretizations. *J. Comput. Phys.*, 337:289–308, May 2017. doi:10.1016/j.jcp.2017.02.039.

[7] J. de Frutos, B. García-Archilla, V. John, and J. Novo. Analysis of the grad-div stabilization for the time-dependent navier–stokes equations with inf-sup stable finite elements. *Adv. Comput. Math.*, 44(1):195–225, 2017. doi:10.1007/s10444-017-9540-1.

[8] D. Durante, C. Pilloton, and A. Colagrossi. Intermittency patterns in the chaotic transition of the planar flow past a circular cylinder. *Phys. Rev. Fluids*, 7(5):054701, 2022. doi:10.1103/physrevfluids.7.054701.

[9] A. El-Shahat, M.-M. Hasan, and Y. Wu. Vortex bladeless wind generator for nano-grids. In *2018 IEEE Global Humanitarian Technology Conference (GHTC)*, pages 1–2. IEEE, 2018. doi:10.1109/GHTC.2018.8601572.

[10] N. Fehn, M. Kronbichler, C. Lehrenfeld, G. Lube, and P. W. Schroeder. High-order DG solvers for under-resolved turbulent incompressible flows: A comparison of L2 and H(div) methods. *Internat. J. Numer. Methods Fluids*, 91(11):533–556, 2019. doi:10.1002/fld.4763.

[11] S. Francis, V. Umesh, and S. Shivakumar. Design and analysis of vortex bladeless wind turbine. *Materials Today: Proceedings*, 47:5584–5588, 2021. doi:10.1016/j.matpr.2021.03.469.

[12] V. Girault and P.-A. Raviart. *Finite Element Methods for Navier–Stokes Equations.* Springer Series in Computational Mathematics, volume 5. Springer–Verlag, Berlin, 1986. doi:10.1007/978-3-642-61623-5.

[13] I. G. Gjerde and L. R. Scott. Resolution of d'Alembert's Paradox using Navier's slip boundary conditions. 2023. doi:10.48550/arXiv.2204.12240.

[14] I. G. Gjerde and L. R. Scott. Verification and validation of cylinder drag: Pressure and stress approximations on curved boundaries. 2023. doi:10.48550/arXiv.2306.12362.

[15] J. Gopalakrishnan, P. L. Lederer, and J. Schöberl. A mass conserving mixed stress formulation for the Stokes equations. *IMA J. Numer. Anal.*, 40(3):1838–1874, 2020. doi:10.1093/imanum/drz022.

[16] J. Gopalakrishnan, P. L. Lederer, and J. Schöberl. A mass conserving mixed stress formulation for Stokes flow with weakly imposed strss symmetry. *SIAM J. Numer. Anal.*, 58(1):706–732, 2020. doi:10.1137/19m1248960.

[17] M. Hayakawa and F. Hussain. Three-dimensionality of organized structures in a plane turbulent wake. *J. Fluid Mech.*, 206:375–404, 1989. doi:10.1017/S0022112089002338.

[18] V. John. Reference values for drag and lift of a two-dimensional time-dependent flow around a cylinder. *Internat. J. Numer. Methods Fluids*, 44(7):777–788, 2004. doi:10.1002/fld.679.

[19] V. John. *Finite element methods for incompressible flow problems.* Springer, Cham, 2016. doi:10.1007/978-3-319-45750-5.

[20] V. John, A. Linke, C. Merdon, M. Neilan, and L. G. Rebholz. On the divergence constraint in mixed finite element methods for incompressible flows. *SIAM Rev.*, 59(3):492–544, Jan. 2017. doi:10.1137/15m1047696.

[21] M. Kornbleuth. *Studying the Viscous Flow Around a Cylinder Using OpenFoam.* PhD thesis, Astronomy Department, Boston University, Boston, MA, USA, 2016.

[22] S. H. Lamb. *Hydrodynamics.* Cambridge University Press, sixth edition, 1932.

[23] A. Linke. On the role of the helmholtz decomposition in mixed methods for incompressible flows and a new variational crime. *Comput. Methods Appl. Mech. Engrg.*, 268:782–800, 2014. doi:10.1016/j.cma.2013.10.011.

[24] A. Linke, L. G. Rebholz, and N. E. Wilson. On the convergence rate of grad-div stabilized taylor–hood to scott–vogelius solutions for incompressible flow problems. *J. Math. Anal. Appl.*, 381(2):612–626, 2011. doi:https://doi.org/10.1016/j.jmaa.2011.03.019.

[25] J. R. Meneghini. *Numerical simulation of bluff body flow control using a discrete vortex method.* PhD thesis, Imperial College London, 1993.

[26] M. Olshanskii, G. Lube, T. Heister, and J. Löwe. Grad–div stabilization and subgrid pressure models for the incompressible navier–stokes equations. *Comput. Methods Appl. Mech. Engrg.*, 198(49):3975–3988, 2009. doi:10.1016/j.cma.2009.09.005.

[27] J. Qin. *On the convergence of some low order mixed finite elements for incompressible fluids.* PhD thesis, Pennsylvania State University, 1994. URL https://www-users.math.umn.edu/~arnold/papers/QinThesis.pdf.

[28] T. Richter. *Fluid-structure Interactions*, volume 118 of *Lecture Notes in Computational Science and Engineering.* Springer, Cham, 2017. doi:10.1007/978-3-319-63970-3.

[29] M. Sahin and R. G. Owens. A numerical investigation of wall effects up to high blockage ratios on two-dimensional flow past a confined circular cylinder. *Phys. Fluids*, 16(5):1305–1320, 2004. doi:10.1063/1.1668285.

[30] M. Schäfer, S. Turek, F. Durst, E. Krause, and R. Rannacher. Benchmark computations of laminar flow around a cylinder. In E. H. Hirschel, editor, *Flow Simulation with High-Performance Computers II: DFG Priority Research Programme Results 1993–1995*, pages 547–566. Vieweg+Teubner Verlag, Wiesbaden, 1996. ISBN 978-3-322-89849-4. doi:10.1007/978-3-322-89849-4_39.

[31] J. Schöberl. NETGEN an advancing front 2D/3D-mesh generator based on abstract rules. *Comput. Vis. Sci.*, 1 (1):41–52, 1997. doi:10.1007/s007910050004.

[32] J. Schöberl. C++11 implementation of finite elements in NGSolve. Technical report, 2014.

[33] P. W. Schroeder and G. Lube. Pressure-robust analysis of divergence-free and conforming FEM for evolutionary incompressible Navier-Stokes flows. *J. Numer. Math.*, 25(4), Dec. 2017. doi:10.1515/jnma-2016-1101.

[34] L. R. Scott. *Introduction to Automated Modeling with FEniCS.* Computational Modeling Initiative, 2018.

[35] L. R. Scott and R. Durst. Chaotic dynamics of two-dimensional flows around a cylinder. *Phys. Fluids*, 36(2): 024118, 2024. doi:10.1063/5.0186496.

[36] L. R. Scott and M. Vogelius. Norm estimates for a maximal right inverse of the divergence operator in spaces of piecewise polynomials. 19(1):111–143, 1985. doi:10.1051/m2an/1985190101111.

[37] M. Vogelius. A right-inverse for the divergence operator in spaces of piecewise polynomials: Application to thep-version of the finite element method. *Numer. Math.*, 41(1):19–37, Feb. 1983. doi:10.1007/bf01396303.

[38] C. H. K. Williamson. Oblique and parallel modes of vortex shedding in the wake of a circular cylinder at low Reynolds numbers. *J. Fluid Mech.*, 206:579–627, 1989. doi:10.1017/S0022112089002429.

[39] C. H. K. Williamson and R. Govardhan. Vortex-induced vibrations. *Annu. Rev. Fluid Mech.*, 36:413–455, 2004. doi:10.1146/annurev.fluid.36.050802.122128.

[40] S. Zhang. A new family of stable mixed finite elements for the 3d stokes equations. *Math. Comp.*, 74(250): 543–555, Aug. 2004. doi:10.1090/s0025-5718-04-01711-9.